INTERNATIONAL JOURNAL FOR NUMERICAL METHODS IN FLUIDS
Int. J. Numer. Meth. Fluids 2013; **71**:1422–1437
Published online 25 July 2012 in Wiley Online Library (wileyonlinelibrary.com/journal/nmf). DOI: 10.1002/fld.3718

Convergence issues in using high-resolution schemes and lower–upper symmetric Gauss–Seidel method for steady shock-induced combustion problems

Bin Li and Li Yuan*,†

LSEC and Institute of Computational Mathematics and Scientific/Engineering Computing, Academy of Mathematics and Systems Science, Chinese Academy of Sciences, Beijing 100190, China

SUMMARY

This paper reports numerical convergence study for simulations of steady shock-induced combustion problems with high-resolution shock-capturing schemes. Five typical schemes are used: the Roe flux-based monotone upstream-centered scheme for conservation laws (MUSCL) and weighted essentially non-oscillatory (WENO) schemes, the Lax–Friedrichs splitting-based non-oscillatory no-free parameter dissipative (NND) and WENO schemes, and the Harten–Yee upwind total variation diminishing (TVD) scheme. These schemes are implemented with the finite volume discretization on structured quadrilateral meshes in dimension-by-dimension way and the lower–upper symmetric Gauss–Seidel (LU–SGS) relaxation method for solving the axisymmetric multispecies reactive Navier–Stokes equations. Comparison of iterative convergence between different schemes has been made using supersonic combustion flows around a spherical projectile with Mach numbers $M = 3.55$ and 6.46 and a ram accelerator with $M = 6.7$. These test cases were regarded as steady combustion problems in literature. Calculations on gradually refined meshes show that the second-order NND, MUSCL, and TVD schemes can converge well to steady states from coarse through fine meshes for $M = 3.55$ case in which shock and combustion fronts are separate, whereas the (nominally) fifth-order WENO schemes can only converge to some residual level. More interestingly, the numerical results show that all the schemes do not converge to steady-state solutions for $M = 6.46$ in the spherical projectile and $M = 6.7$ in the ram accelerator cases on fine meshes although they all converge on coarser meshes or on fine meshes without chemical reactions. The result is based on the particular preconditioner of LU–SGS scheme. Possible reasons for the nonconvergence in reactive flow simulation are discussed. Copyright © 2012 John Wiley & Sons, Ltd.

Received 5 October 2011; Revised 14 June 2012; Accepted 1 July 2012

KEY WORDS: high-resolution scheme; supersonic combustion; detonative wave; steady solution; grid independence

1. INTRODUCTION

The shock-induced combustion is caused by the shock wave compressing the fuel-oxidant mixture. It has great technological interest in aerospace and other industry fields as it frequently occurs in scramjet engines, pulse detonation engines [1], and explosion of energetic materials and coal gas [2]. Numerical simulation of shock-induced combustion is confronted with many difficulties common to chemically reacting flow simulation, such as stiffness because of different characteristic scales, complex hydrodynamic–chemical interactions, a great amount of computational cost, and the particular difficulty that detonation waves occurring in some situations are very sensitive to

*Correspondence to: Li Yuan, LSEC and Institute of Computational Mathematics and Scientific/Engineering Computing, Academy of Mathematics and Systems Science, Chinese Academy of Sciences, Beijing 100190, China.
†E-mail: lyuan@lsec.cc.ac.cn

modeling setups and numerical errors [3]. Therefore, reliable numerical methods for shock-induced combustion problems are required for practical applications.

Although shock-induced combustion may occur in many different configurations and exhibit unsteady states, the focus in this paper is on the steady-state problems of supersonic premixed hydrogen/oxygen (air) flows past axisymmetric projectiles in a free stream or in a pipe, where a bow shock or oblique shock is formed to induce combustion. This type of shock-induced combustion problems has been studied over the years, including both experiments [4, 5] and numerical simulations [6–9] to mention but a few contributions. The steady-state solutions serve to test the convergence property of high-resolution schemes before they can be used to simulate engineering combustion reliably.

High-resolution shock-capturing schemes for hyperbolic conservation laws are widely used for numerical simulation of compressible inviscid and viscous flows. Most of them have been directly applied to solve combustion problems, including total variation diminishing (TVD) schemes [10, 11], monotone upstream-centered schemes for conservation laws (MUSCL) [12, 13], non-oscillatory no-free parameter dissipative (NND) [14, 15], essentially non-oscillatory (ENO) and weighted ENO (WENO) schemes [16–20], advection upstream splitting method (AUSM) [21, 22], space-time conservation element and solution element method [23, 24], and discontinuous Galerkin methods [25–27] to mention but some work. Although these schemes have been well tested in conservation laws and nonreacting flows, they are worthwhile to be further checked and developed for computing steady shock-induced combustion problems. Recent developments of high-resolution schemes have emphasized on high-order accuracy [28] and subcell resolution [20]. Although these new methods are shown to be good at modeling reaction and diffusion zones [20, 29], it is also meaningful to see whether they converge well in computing steady shock-induced combustion problems, which is important for engineering design.

In this paper, we study convergence-to-steady state issues encountered when using high-resolution schemes to compute steady shock-induced combustion problems. In [9], we have shown that TVD scheme does not converge to steady state on fine meshes for the shock-induced combusting flow around a spherical projectile with Mach number of 6.46 even though it converges on medium-sized meshes. To show that this convergence difficulty is not specific with one specific scheme, five widely used high-resolution schemes are studied in this work. The first and second schemes are based on the Roe approximate Riemann solver [30], with second-order MUSCL [12] and fifth-order WENO reconstructions [31] respectively for characteristic variables (hereafter referred to as MUSCL-Roe and WENO-Roe), the third and fourth schemes are based on the local Lax–Friedrichs (LF) splitting in characteristic decomposition, with second-order NND [14] and fifth-order WENO reconstructions [32] respectively for the split fluxes (NND-LF and WENO-LF), and the fifth scheme is the Harten–Yee second-order upwind TVD scheme [33] already tested in [9]. We use finite volume discretization for these schemes on structured quadrilateral meshes. As a genuinely two-dimensional finite volume WENO scheme is complicated to construct, we simply implement the WENO scheme similar to the finite difference version, that is, in dimension-by-dimension way. This will not generally give fifth-order accuracy on general quadrilateral meshes even if we use the fifth-order WENO reconstruction in each direction. However, we believe that this implementation will represent the convergence-to-steady state behavior of genuinely fifth-order accurate finite volume WENO schemes. Time derivatives are discretized with backward difference, and the linearized algebraic equations are solved with the lower–upper symmetric Gauss–Seidel (LU–SGS) relaxation scheme [34, 35]. Numerical results for supersonic premixed hydrogen/oxygen (air) flows past a spherical projectile [4] and a ram accelerator [6] are presented. The selected cases correspond to steady-state ones in [4, 6]. As there were a few numerical simulations of these steady-state cases [6–9], we take a further step in which we hope to obtain grid-independent solutions with each of the five schemes. The mesh resolutions are varied from 256^2 to 1024^2. Contrary to our expectation, the numerical results show that all the five schemes have convergence difficulties in computing some steady shock-induced combustion problems on fine meshes. We then discuss possible reasons behind this numerical behavior.

This paper is organized as follows. In Section 2, we present the governing equations and reaction mechanisms for supersonic chemically reacting viscous flows. Five high-resolution schemes

DOI: 10.1002/fld

are described in Section 3. Numerical simulations of steady shock-induced combustion problems are given with some discussions in Section 4. Conclusions are presented in Section 5.

2. GOVERNING EQUATIONS

The governing equations for axisymmetric chemically reacting viscous flows are the compressible Navier–Stokes equations with chemical source terms for a mixture of N gas species, which can be written in nondimensional form in cylindrical coordinates as

$$\frac{\partial \mathbf{U}}{\partial t}+\frac{\partial \mathbf{F}}{\partial x}+\frac{\partial \mathbf{G}}{\partial y}=\frac{1}{\mathrm{Re}}\left(\frac{\partial \mathbf{F}_v}{\partial x}+\frac{\partial \mathbf{G}_v}{\partial y}\right)+\mathbf{H}+\frac{1}{\mathrm{Re}}\mathbf{H}_v+\mathbf{S}, \tag{1}$$

where

$$\mathbf{U}=[\rho_1,\ldots,\rho_N,\rho u,\rho v,\rho E]^{\mathrm{T}}, \tag{2}$$

$$\mathbf{F}=\left[\rho_1 u,\ldots,\rho_N u,\rho u^2+p,\rho uv,u\left(\rho E+p\right)\right]^{\mathrm{T}}, \tag{3}$$

$$\mathbf{G}=\left[\rho_1 v,\ldots,\rho_N v,\rho uv,\rho v^2+p,v\left(\rho E+p\right)\right]^{\mathrm{T}}, \tag{4}$$

$$\mathbf{F}_v=\left[\rho D_1\frac{\partial Y_1}{\partial x},\ldots,\rho D_N\frac{\partial Y_N}{\partial x},\tau_{xx},\tau_{xy},u\tau_{xx}+v\tau_{xy}-q_x\right]^{\mathrm{T}}, \tag{5}$$

$$\mathbf{G}_v=\left[\rho D_1\frac{\partial Y_1}{\partial y},\ldots,\rho D_N\frac{\partial Y_N}{\partial y},\tau_{xy},\tau_{yy},u\tau_{xy}+v\tau_{yy}-q_y\right]^{\mathrm{T}}, \tag{6}$$

$$\mathbf{H}=-\frac{1}{y}\left[\rho_1 v,\ldots,\rho_N v,\rho uv,\rho v^2,v\left(\rho E+p\right)\right]^{\mathrm{T}}, \tag{7}$$

$$\mathbf{H}_v=\frac{1}{y}\left[\rho D_1\frac{\partial Y_1}{\partial y},\ldots,\rho D_N\frac{\partial Y_N}{\partial y},\tau_{xy},\tau_{yy}-\tau_{\theta\theta},u\tau_{xy}+v\tau_{yy}-q_y\right]^{\mathrm{T}}, \tag{8}$$

$$\mathbf{S}=\frac{L}{\rho_\infty u_\infty}\left[\dot{\omega}_1,\ldots,\dot{\omega}_N,0,0,0\right]^{\mathrm{T}}, \tag{9}$$

and

$$\tau_{xx}=2\mu\frac{\partial u}{\partial x}-\frac{2}{3}\mu\nabla\cdot\mathbf{u}=\frac{2}{3}\mu\left(2\frac{\partial u}{\partial x}-\frac{\partial v}{\partial y}-\frac{v}{y}\right), \tag{10}$$

$$\tau_{yy}=2\mu\frac{\partial v}{\partial y}-\frac{2}{3}\mu\nabla\cdot\mathbf{u}=\frac{2}{3}\mu\left(2\frac{\partial v}{\partial y}-\frac{\partial u}{\partial x}-\frac{v}{y}\right), \tag{11}$$

$$\tau_{xy}=\mu\left(\frac{\partial u}{\partial y}+\frac{\partial v}{\partial x}\right), \tag{12}$$

$$\tau_{\theta\theta}=2\mu\frac{v}{y}-\frac{2}{3}\mu\nabla\cdot\mathbf{u}=\frac{2}{3}\mu\left(2\frac{v}{y}-\frac{\partial u}{\partial x}-\frac{\partial v}{\partial y}\right), \tag{13}$$

$$q_x=-\kappa\frac{\partial T}{\partial x}-\rho\sum_{k=1}^{N}h_k D_k\frac{\partial Y_k}{\partial x}, \tag{14}$$

$$q_y=-\kappa\frac{\partial T}{\partial y}-\rho\sum_{k=1}^{N}h_k D_k\frac{\partial Y_k}{\partial y}. \tag{15}$$

Here, ρ_k is the partial density of the kth species, ρ is the total density of the gas mixture, Y_k is the mass fraction of the kth species, u and v are velocity components in the axial x and radial y directions, respectively, p is the pressure, T is the temperature, E is the total energy per unit mass, h_k is the specific enthalpy and $\dot{\omega}_k$ is the mass production rate of the kth species, D_k is the effective mass diffusivity of the kth species in the mixture, and μ and κ are the viscosity and thermal conductivity of the mixture. The governing equations are nondimensionalized by a reference length

DOI: 10.1002/fld

L and the free-stream velocity u_∞, density ρ_∞, and viscosity μ_∞. The Reynolds number is defined as $\mathrm{Re} = \rho_\infty u_\infty L/\mu_\infty$. However, for clarity, dimensional forms are used in Sections 2.1–2.3.

2.1. Thermodynamic properties

In the present chemical nonequilibrium system, it is assumed that every species is a thermally perfect gas, so that all species have the same temperature. The system is closed with the equation of state of the ideal gas mixture,

$$p = \rho \mathcal{R} T \sum_{k=1}^{N} \frac{Y_k}{M_k}, \tag{16}$$

where $\mathcal{R}$ is the universal gas constant and M_k is the molecular mass of the kth species. The molar heat capacity C_{p_k} of the kth species at constant pressure is a given function of temperature in polynomial fit

$$C_{p_k} = \mathcal{R} \sum_{i=1}^{5} a_{ik} T^{i-1}, \tag{17}$$

where the coefficients a_{ik} can be found from the thermodynamic data file of the chemical kinetics package [36] or from NASA thermochemical polynomial data [37]. Given C_{p_k}, the specific heat and the enthalpy of the kth species can be computed from

$$c_{p_k} = \frac{C_{p_k}}{M_k}, \qquad h_k(T) = \int_{T_{\mathrm{ref}}}^{T} c_{p_k}(T')\, dT' + h_k^{\mathrm{ref}}, \tag{18}$$

where h_k^{ref} is the heat of formation at the reference temperature T_{ref} usually taken as 298.15 K. The specific heat and enthalpy of the gas mixture are then given by

$$c_p = \sum_{k=1}^{N} Y_k c_{p_k}, \qquad h = \sum_{k=1}^{N} Y_k h_k. \tag{19}$$

The temperature T can be computed from the thermodynamic relationship

$$\rho E - \frac{1}{2}\rho \left(u^2 + v^2\right) = \sum_{k=1}^{N} \rho_k h_k - p. \tag{20}$$

As h_k is a segmented quintic polynomial of temperature, evaluation of temperature can be obtained by linear interpolation of a precalculated $T - h_k(T)$ table instead of implicit iteration for simplicity. The frozen speed of sound of the gas mixture is

$$a = \sqrt{\gamma R T} \tag{21}$$

with the specific heat ratio $\gamma = c_p/(c_p - R)$ and the mixture gas constant $R = \mathcal{R} \sum_{k=1}^{N} Y_k/M_k$.

2.2. Transport properties

The viscosity μ of the gas mixture is given by Wilke formula as

$$\mu = \sum_{k=1}^{N} \left(\frac{X_k \mu_k}{\sum_{j=1}^{N} X_j \phi_{kj}} \right), \tag{22}$$

where μ_k is the viscosity and X_k is the mole fraction of the kth species, and the allocation function is

$$\phi_{kj} = \left[1 + \left(\frac{\mu_k}{\mu_j} \right)^{1/2} \left(\frac{M_j}{M_k} \right)^{1/4} \right]^2 \left[\sqrt{8} \left(1 + \frac{M_k}{M_j} \right)^{1/2} \right]^{-1}. \tag{23}$$

DOI: 10.1002/fld

The individual viscosity μ_k in International System of Units is given by an empirical fit

$$\mu_k = 0.1 \exp\left(A_{\mu_k} \ln^2 T + B_{\mu_k} \ln T + C_{\mu_k}\right) \tag{24}$$

with the curve-fit coefficients A_{μ_k}, B_{μ_k}, C_{μ_k} found from NASA thermodynamic data [37, 38].

The thermal conductivity κ of the gas mixture is obtained from the viscosity by assuming a constant Prandtl number for the gas mixture,

$$\kappa = \frac{\mu c_p}{\mathrm{Pr}}, \tag{25}$$

where Pr is the Prandtl number that is set to 0.71 in this study. The mass diffusivity D_k is computed using an effective diffusivity by neglecting pressure diffusion and Soret effect and assuming equal binary diffusivity among all component pairs. For simplicity, its value is obtained by assuming a constant Schmidt number $\mathrm{Sc} = \mu/\rho D_k = 0.5$.

2.3. Chemical kinetics

Consider a chemical reaction system involving N species and I elementary reactions represented as

$$\sum_{k=1}^{N} \nu'_{ki} \chi_k \rightleftharpoons \sum_{k=1}^{N} \nu''_{ki} \chi_k, \quad i = 1, \cdots, I, \tag{26}$$

where ν'_{ki} and ν''_{ki} are the forward and reverse stoichiometric coefficients of the kth species χ_k in the ith reaction, respectively. The mass production rate of the kth species can be expressed as

$$\dot{\omega}_k = M_k \sum_{i=1}^{I} \left(\nu''_{ki} - \nu'_{ki}\right) q_i, \quad k = 1, \cdots, N. \tag{27}$$

The rate of progress variable q_i for the ith reaction is given by

$$q_i = \left(\sum_{k=1}^{N} (\alpha_{ki}) \left(\frac{\rho_k}{M_k}\right)\right)^{L_i} \left(k_{f_i} \prod_{k=1}^{N} \left(\frac{\rho_k}{M_k}\right)^{\nu'_{ki}} - k_{r_i} \prod_{k=1}^{N} \left(\frac{\rho_k}{M_k}\right)^{\nu''_{ki}}\right). \tag{28}$$

α_{ki} is the contribution factor of the kth species as a third body, and L_i is equal to one when a third body appears in the ith reaction; otherwise, L_i is equal to zero. By using the Arrhenius law

$$k_i = A_i T^{B_i} \exp\left(-\frac{C_i}{T}\right), \tag{29}$$

we can obtain the forward and reverse reaction rate constants k_{f_i} and k_{r_i} for the ith reaction.

3. NUMERICAL METHOD

Let $\overline{\mathbf{U}}$ denote the cell average of $\mathbf{U}$ over a control volume Ω

$$\overline{\mathbf{U}} = \frac{1}{|\Omega|} \int_{\Omega} \mathbf{U} dV. \tag{30}$$

By integrating the governing equations (1) over Ω and using the Stokes formula, one can obtain

$$|\Omega| \frac{d\overline{\mathbf{U}}}{dt} + \oint_{\partial\Omega} \left(\vec{\mathbf{f}} \cdot \vec{n}\right) dS = \int_{\Omega} \left(\mathbf{H} + \frac{1}{\mathrm{Re}} \mathbf{H}_v + \mathbf{S}\right) dV, \tag{31}$$

where $\vec{\mathbf{f}} = \left(\mathbf{F} - \frac{1}{\mathrm{Re}} \mathbf{F}_v\right) \mathbf{i} + \left(\mathbf{G} - \frac{1}{\mathrm{Re}} \mathbf{G}_v\right) \mathbf{j}$ and $\vec{n}$ is the unit outer normal.

DOI: 10.1002/fld

Assuming that Ω is a quadrilateral mesh, the surface integration in (31) is approximated by some numerical fluxes, and the volume integration is approximated by values at the cell center, we can obtain the semidiscretized form

$$\begin{aligned}\left(|\Omega|\frac{\partial \overline{\mathbf{U}}}{\partial t}\right)_{i,j}+\left(\hat{\mathbf{F}}_{i+\frac{1}{2}}-\hat{\mathbf{F}}_{i-\frac{1}{2}}\right)_j+\left(\hat{\mathbf{G}}_{j+\frac{1}{2}}-\hat{\mathbf{G}}_{j-\frac{1}{2}}\right)_i=\left(\hat{\mathbf{F}}_{v,i+\frac{1}{2}}-\hat{\mathbf{F}}_{v,i-\frac{1}{2}}\right)_j\\ +\left(\hat{\mathbf{G}}_{v,j+\frac{1}{2}}-\hat{\mathbf{G}}_{v,j-\frac{1}{2}}\right)_i+\left[|\Omega|\left(\mathbf{H}+\frac{1}{\mathrm{Re}}\mathbf{H}_v+\mathbf{S}\right)\right]_{i,j}.\end{aligned} \tag{32}$$

By applying the backward time difference and approximate linearization treatment as in [9, 34, 35], we obtain the fully discretized incremental form

$$\begin{aligned}&\left(\frac{|\Omega|}{\Delta t}\mathbf{I}-|\Omega|\mathbf{P}_{i,j}+\mathbf{A}^+_{i,j}-\mathbf{A}^-_{i,j}+\mathbf{B}^+_{i,j}-\mathbf{B}^-_{i,j}+\mathbf{A}^{v,i-\frac{1}{2}}_{i,j}+\mathbf{A}^{v,i+\frac{1}{2}}_{i,j}+\mathbf{B}^{v,j-\frac{1}{2}}_{i,j}\right.\\ &\left.+\mathbf{B}^{v,j+\frac{1}{2}}_{i,j}\right)\Delta\mathbf{U}_{i,j}-\left(\mathbf{A}^+_{i-1}+\mathbf{A}^{v,i-\frac{1}{2}}_{i-1}\right)_j\Delta\mathbf{U}_{i-1,j}+\left(\mathbf{A}^-_{i+1}-\mathbf{A}^{v,i+\frac{1}{2}}_{i+1}\right)_j\Delta\mathbf{U}_{i+1,j}\\ &-\left(\mathbf{B}^+_{j-1}+\mathbf{B}^{v,j-\frac{1}{2}}_{j-1}\right)_i\Delta\mathbf{U}_{i,j-1}+\left(\mathbf{B}^-_{j+1}-\mathbf{B}^{v,j+\frac{1}{2}}_{j+1}\right)_i\Delta\mathbf{U}_{i,j+1}=\mathrm{RHS}^n,\end{aligned} \tag{33}$$

where $\Delta\mathbf{U}_{i,j}=\overline{\mathbf{U}}^{n+1}_{i,j}-\overline{\mathbf{U}}^{n}_{i,j}$, $\mathbf{P}=\partial\mathbf{S}/\partial\mathbf{U}$, $\mathbf{A}^{\pm}=0.5(\mathbf{A}\pm\lambda^{A}_{\max}\mathbf{I})$, $\mathbf{A}=\partial\hat{\mathbf{F}}/\partial\mathbf{U}$, $\mathbf{A}^{v,i-1/2}_{i-1,j}=-\dfrac{\partial\hat{\mathbf{E}}_{v,i-1/2}}{\partial\mathbf{U}_{i-1}}$, $\mathbf{A}^{v,i-1/2}_{i,j}=\dfrac{\partial\hat{\mathbf{E}}_{v,i-1/2}}{\partial\mathbf{U}_{i}}$, $\mathbf{A}^{v,i+1/2}_{i,j}=-\dfrac{\partial\hat{\mathbf{E}}_{v,i+1/2}}{\partial\mathbf{U}_{i}}$, $\mathbf{A}^{v,i+1/2}_{i+1,j}=\dfrac{\partial\hat{\mathbf{E}}_{v,i+1/2}}{\partial\mathbf{U}_{i+1}}$, and

$$\begin{aligned}\mathrm{RHS}^n=&-\left(\hat{\mathbf{F}}_{i+\frac{1}{2}}-\hat{\mathbf{F}}_{i-\frac{1}{2}}\right)^n_j-\left(\hat{\mathbf{G}}_{j+\frac{1}{2}}-\hat{\mathbf{G}}_{j-\frac{1}{2}}\right)^n_i+\left(\hat{\mathbf{F}}_{v,i+\frac{1}{2}}-\hat{\mathbf{F}}_{v,i-\frac{1}{2}}\right)^n_j\\ &+\left(\hat{\mathbf{G}}_{v,j+\frac{1}{2}}-\hat{\mathbf{G}}_{v,j-\frac{1}{2}}\right)^n_i+\left[|\Omega|\left(\mathbf{H}+\frac{1}{\mathrm{Re}}\mathbf{H}_v+\mathbf{S}\right)\right]^n_{i,j}.\end{aligned} \tag{34}$$

Equation (33) can be solved with the conventional LU–SGS relaxation scheme.

The central difference is used to approximate the diffusive flux $\hat{\mathbf{F}}_v(\hat{\mathbf{G}}_v)$, and five high-resolution schemes are used respectively to approximate the inviscid flux $\hat{\mathbf{F}}(\hat{\mathbf{G}})$ in RHS^n, which are described in the following.

3.1. Schemes based on Roe approximate Riemann solver

A numerical flux across the cell interface may be determined by solving exactly or approximately a Riemann problem. We choose the numerical flux because of Roe approximate Riemann solver

$$\hat{\mathbf{F}}^{\mathrm{Roe}}_{i+\frac{1}{2}}=\frac{1}{2}\left(\mathbf{F}\left(\mathbf{U}^L_{i+\frac{1}{2}}\right)+\mathbf{F}\left(\mathbf{U}^R_{i+\frac{1}{2}}\right)\right)-\frac{1}{2}\left|\overline{\mathbf{A}}\left(\mathbf{U}^L_{i+\frac{1}{2}},\mathbf{U}^R_{i+\frac{1}{2}}\right)\right|\left(\mathbf{U}^R_{i+\frac{1}{2}}-\mathbf{U}^L_{i+\frac{1}{2}}\right), \tag{35}$$

where $\mathbf{F}$ denotes the physical flux normal to the cell interface, and matrix $\overline{\mathbf{A}}$ is the inviscid Jacobian matrix $\mathbf{A}=\partial\mathbf{F}/\partial\mathbf{U}$ evaluated at Roe average of the left and right states of the cell interface $i+1/2$. It is well known that this flux admits nonphysical expansion shock. This can be mitigated by modifying the magnitude of the eigenvalue $\lambda_{i+1/2}$ of $\overline{\mathbf{A}}$ as the following [10]:

$$\psi\left(\lambda_{i+1/2}\right)=\begin{cases}\left|\lambda_{i+1/2}\right|, & \left|\lambda_{i+1/2}\right|\geqslant\delta,\\ \dfrac{\lambda^2_{i+1/2}+\delta^2}{2\delta}, & \left|\lambda_{i+1/2}\right|<\delta.\end{cases} \tag{36}$$

where δ is the entropy correction parameter, the choice of which is critical for calculating steady-state problems containing strong shocks. We have used two choices. One is so-called H-type correction due to Sanders [39]

$$\delta=S_{i+\frac{1}{2}}\max\left(\epsilon_{i+\frac{1}{2},j},\,\epsilon_{i,j\pm\frac{1}{2}},\,\epsilon_{i+1,j\pm\frac{1}{2}}\right), \tag{37}$$

DOI: 10.1002/fld

where $S_{i+\frac{1}{2}}$ is the surface area and

$$\epsilon_{i+\frac{1}{2},j} = \left|\hat{u}_{i+1,j} - \hat{u}_{i,j}\right| + \left|a_{i+1,j} - a_{i,j}\right|, \quad \epsilon_{i,j+\frac{1}{2}} = \left|\hat{u}_{i,j+1} - \hat{u}_{i,j}\right| + \left|a_{i,j+1} - a_{i,j}\right|.$$

Here, $\hat{u}$ is the velocity component normal to the respective interface. The other is adopted from the code LAURA user's manual [40]

$$\delta = S_{i+\frac{1}{2}} \begin{cases} \max\left(0.02\left(|\hat{u}_{i+\frac{1}{2}}| + |\hat{v}_{i+\frac{1}{2}}|\right), 0.002a_{i+\frac{1}{2}}\right), & \lambda = \hat{u}_{i+\frac{1}{2}} \\ \epsilon_0\left(a_{i+\frac{1}{2}} + |\hat{u}_{i+\frac{1}{2}}| + |\hat{v}_{i+\frac{1}{2}}|\right), & \text{otherwise} \end{cases} \tag{38}$$

where ϵ_0 is a user-defined constant that generally varies from 0.02 to 0.6 [40], and $\hat{u}_{i+1/2}$ and $\hat{v}_{i+1/2}$ are the normal and tangential velocity components at the interface $i + 1/2$, respectively. The first line of (38) is used only for the multiple eigenvalues $\lambda = \hat{u}_{j+1/2}$ in the normal-to-body (j) direction. Equation (38) is used only for $M = 3.55$ flow around the spherical projectile to better cure the carbuncle-like abnormality of the combustion front, whereas the H-type correction is used for all other cases.

For MUSCL-Roe scheme, we employ the second-order MUSCL reconstruction [12] from the cell averaged values

$$\begin{aligned} \mathbf{U}^L_{i+\frac{1}{2}} &= \mathbf{U}_i + \frac{1}{2}\mathbf{R}^*_{i+\frac{1}{2}}\phi\left(\Delta\mathbf{W}_{i-\frac{1}{2}}, \Delta\mathbf{W}_{i+\frac{1}{2}}\right), \\ \mathbf{U}^R_{i+\frac{1}{2}} &= \mathbf{U}_{i+1} - \frac{1}{2}\mathbf{R}^*_{i+\frac{1}{2}}\phi\left(\Delta\mathbf{W}_{i+\frac{1}{2}}, \Delta\mathbf{W}_{i+\frac{3}{2}}\right). \end{aligned} \tag{39}$$

The limiter function $\phi(a, b)$ is a minmod function, and the differences of the characteristic variables are

$$\Delta\mathbf{W}_{k+\frac{1}{2}} = \mathbf{R}^{*-1}_{i+\frac{1}{2}}\left(\mathbf{U}_{k+1} - \mathbf{U}_k\right), \quad i - 1 \leqslant k \leqslant i + 1. \tag{40}$$

Unlike simple average between $\mathbf{U}_i$ and $\mathbf{U}_{i+1}$ as in previous literature [31], we use Roe average of $\mathbf{U}^{L*}_{i+1/2}$ and $\mathbf{U}^{R*}_{i+1/2}$ to compute eigenvector matrices $\mathbf{R}^*_{i+1/2}$ and $\mathbf{R}^{*-1}_{i+1/2}$ needed for characteristic decomposition. The '$*$' states are computed using component-by-component reconstruction of conservative variables

$$\mathbf{U}^{L*}_{i+\frac{1}{2}} = \mathbf{U}_i + \frac{1}{2}\phi\left(\Delta\mathbf{U}_{i-\frac{1}{2}}, \Delta\mathbf{U}_{i+\frac{1}{2}}\right), \ \mathbf{U}^{R*}_{i+\frac{1}{2}} = \mathbf{U}_{i+1} - \frac{1}{2}\phi\left(\Delta\mathbf{U}_{i+\frac{1}{2}}, \Delta\mathbf{U}_{i+\frac{3}{2}}\right). \tag{41}$$

Numerical tests with $M = 6.46$ indicate that this choice can prevent residuals flattening for MUSCL-Roe scheme on coarse meshes.

For WENO-Roe scheme, we employ the one-dimensional fifth-order WENO reconstruction for the left and right states of the interface according to [32, 41]:

$$\begin{aligned} \mathbf{U}^L_{i+\frac{1}{2}} = \frac{1}{12}&\left(-\mathbf{U}_{i-1} + 7\mathbf{U}_i + 7\mathbf{U}_{i+1} - \mathbf{U}_{i+2}\right) - \\ &\mathbf{R}_{i+\frac{1}{2}}\varphi\left(\Delta\mathbf{W}_{i-\frac{3}{2}}, \Delta\mathbf{W}_{i-\frac{1}{2}}, \Delta\mathbf{W}_{i+\frac{1}{2}}, \Delta\mathbf{W}_{i+\frac{3}{2}}\right), \\ \mathbf{U}^R_{i+\frac{1}{2}} = \frac{1}{12}&\left(-\mathbf{U}_{i-1} + 7\mathbf{U}_i + 7\mathbf{U}_{i+1} - \mathbf{U}_{i+2}\right) + \\ &\mathbf{R}_{i+\frac{1}{2}}\varphi\left(\Delta\mathbf{W}_{i+\frac{5}{2}}, \Delta\mathbf{W}_{i+\frac{3}{2}}, \Delta\mathbf{W}_{i+\frac{1}{2}}, \Delta\mathbf{W}_{i-\frac{1}{2}}\right). \end{aligned} \tag{42}$$

The nonlinear function φ is defined as

$$\varphi(a, b, c, d) = \frac{1}{3}\omega_0(a - 2b + c) + \frac{1}{6}\left(\omega_2 - \frac{1}{2}\right)(b - 2c + d), \tag{43}$$

DOI: 10.1002/fld

with the nonlinear weights given by

$$\omega_0 = \frac{\alpha_0}{\alpha_0 + \alpha_1 + \alpha_2}, \quad \omega_2 = \frac{\alpha_2}{\alpha_0 + \alpha_1 + \alpha_2}, \tag{44}$$

$$\alpha_0 = \frac{1}{(\varepsilon + \mathrm{IS}_0)^2}, \ \alpha_1 = \frac{6}{(\varepsilon + \mathrm{IS}_1)^2}, \ \alpha_2 = \frac{3}{(\varepsilon + \mathrm{IS}_2)^2}, \tag{45}$$

$$\begin{gathered} \mathrm{IS}_0 = 13(a-b)^2 + 3(a-3b)^2, \ \ \mathrm{IS}_1 = 13(b-c)^2 + 3(b+c)^2, \\ \mathrm{IS}_2 = 13(c-d)^2 + 3(3c-d)^2. \end{gathered} \tag{46}$$

Remark on ε. The numerical effect of this parameter has been discussed in [42]. Because the left eigenvectors are differently scaled so as to affect smoothness indicator IS_k, ε is tuned in $10^{-6} \sim 10^{-9}$ in the present work.

3.2. Schemes based on local Lax–Friedrichs splitting

Let $\mathbf{l}^s_{i+1/2}$ denote the sth left eigenvector of the Jacobian matrix $\mathbf{A}_{i+1/2}$ and $\mathbf{r}^s_{i+1/2}$ that denote the sth right eigenvector. The left eigenvector is a row vector, and the right eigenvector is a column vector. The eigenvectors can be evaluated using simple average between $\mathbf{U}_i$ and $\mathbf{U}_{i+1}$ [31]. Given $\mathbf{l}_{i+1/2}$, the inviscid flux and conservative variables can be projected into the eigenvector space as follows:

$$f^s_k = \mathbf{l}^s_{i+\frac{1}{2}} \cdot \mathbf{F}_k, \qquad w^s_k = \mathbf{l}^s_{i+\frac{1}{2}} \cdot \mathbf{U}_k, \quad 1 \leqslant s \leqslant m, \quad i-1 \leqslant k \leqslant i+2, \tag{47}$$

where m is the number of components of vector $\mathbf{U}$. The local Lax–Friedrichs splitting of the characteristic component flux is

$$f^{s,\pm}_k = \frac{1}{2}\left(f^s_k \pm \psi\left(\lambda^s\right) w^s_k\right), \tag{48}$$

where $\psi(\lambda)$ is the entropy fix function (36) and $\lambda^s = \max_{i-1\leqslant k\leqslant i+2} \left|\lambda^s_k\right|$ is the sth maximum eigenvalue over the relevant stencil of NND scheme [14]. After the characteristic numerical fluxes are constructed with MUSCL formula (41), they are transformed back to the physical space to obtain NND-LF scheme

$$\begin{aligned} \hat{\mathbf{F}}^{\text{NND-LF}}_{i+\frac{1}{2}} = {} & \frac{1}{2}\left(\mathbf{F}_i + \mathbf{F}_{i+1}\right) \\ & + \frac{1}{2}\sum_{s=1}^{m}\left[\phi\left(\Delta f^{s,+}_{i-\frac{1}{2}}, \Delta f^{s,+}_{i+\frac{1}{2}}\right) - \phi\left(\Delta f^{s,-}_{i+\frac{1}{2}}, \Delta f^{s,-}_{i+\frac{3}{2}}\right) - \lambda^s \Delta w^s_{i+\frac{1}{2}}\right]\mathbf{r}^s_{i+\frac{1}{2}}, \end{aligned} \tag{49}$$

where $\Delta f^{s,\pm}_{k+1/2} = f^{s,\pm}_{k+1} - f^{s,\pm}_k$, $\quad i-1 \leqslant k \leqslant i+1$. Similarly, one can obtain WENO-LF scheme [32]

$$\begin{aligned} \hat{\mathbf{F}}^{\text{WENO-LF}}_{i+\frac{1}{2}} = {} & \frac{1}{12}\left(-\mathbf{F}_{i-1} + 7\mathbf{F}_i + 7\mathbf{F}_{i+1} - \mathbf{F}_{i+2}\right) - \sum_{s=1}^{m}\left[\varphi\left(\Delta f^{s,+}_{i-\frac{3}{2}}, \Delta f^{s,+}_{i-\frac{1}{2}}, \Delta f^{s,+}_{i+\frac{1}{2}}, \Delta f^{s,+}_{i+\frac{3}{2}}\right)\right. \\ & \left. - \varphi\left(\Delta f^{s,-}_{i+\frac{5}{2}}, \Delta f^{s,-}_{i+\frac{3}{2}}, \Delta f^{s,-}_{i+\frac{1}{2}}, \Delta f^{s,-}_{i-\frac{1}{2}}\right)\right]\mathbf{r}^s_{i+\frac{1}{2}}. \end{aligned} \tag{50}$$

where $\lambda^s = \max_{i-2\leqslant k\leqslant i+3} \left|\lambda^s_k\right|$.

The fifth scheme used in this paper is the well-known Harten–Yee second-order upwind TVD scheme [33]. For details, see [33] or [9].

DOI: 10.1002/fld

3.3. Boundary treatment

To compute the numerical flux on boundaries, ghost cells outside the computational domain are used. The values of ghost cells depend on specific boundary conditions. On the supersonic inflow boundary, the ghost values are set to free-stream values, whereas on the supersonic outflow boundary, they are constantly extrapolated. On the body wall, nonslip, isothermal or adiabatic, and noncatalytic conditions are used to determine the first ghost cell for evaluating the viscous flux and the physical flux on the boundary, but reflection boundary conditions are utilized to obtain ghost values for evaluating dissipation terms in all schemes. Reflection conditions are used on the symmetry axis to determine ghost cells. Geometric metrics of all ghost cells are determined according to reflection from corresponding inner cells.

4. NUMERICAL RESULTS

Two shock-induced combustion problems for a spherical projectile and a ram accelerator are considered in this study. Five different mesh sizes, which are 256^2, 384^2, 512^2, 768^2, and 1024^2, are used. We call mesh size $\geqslant 512^2$ as fine meshes, $\leqslant 256^2$ as coarse meshes, and in between as medium meshes. Computation is assumed to reach steady state when residuals drop by three orders of magnitude.

4.1. External flows past a spherical projectile

A spherical projectile with 15 mm diameter was shot into the explosive gas mixtures of H_2/O_2 ($2H_2 + O_2$) at the speed of 1892 m/s and of H_2/air($2H_2 + O_2 + 3.76N_2$) at the speed of 2605 m/s respectively corresponding to Figures 1 and 5 in Lehr's benchmark experiments [4]. For simplicity, the computational domain covers only the hemisphere. The incoming flow conditions for the two cases are summarized in Table I. The inlet boundary conditions are free-stream states, whereas the supersonic outflow boundary conditions are zero derivative for flow variables. Nonslip, adiabatic, and noncatalytic boundary conditions are enforced on the body surface. Symmetric flow conditions are applied at the symmetric axis. Both of the two cases are initialized from the free-stream condition. We adopt Evans' seven-species 16-reactions model for H_2/O_2 mixture combustion and eight-species 16-reactions model for H_2/air mixture combustion [43] in our simulation. The reaction model is processed with the chemical kinetics package chemical kinetics.

Figure 1(a) shows comparison of convergence history of the five schemes for $M = 3.55$ case on the 256^2 mesh. For all schemes, equation (38) is used with $\epsilon_0 = 0.4$ to suppress the carbuncle-like phenomenon on the combustion front. It can be seen that NND-LF, MUSCL-Roe, and TVD schemes converge well. WENO-LF converges a little bit slower, whereas WENO-Roe is slowest and halts above 10^{-5} after dropping by three orders of magnitude. Figure 1(b) shows convergence histories on the 512^2 mesh. It is seen that WENO-LF can converge to small residual, whereas WENO-Roe can only halt at 10^{-5}. Although not shown here, all schemes have similar convergence behavior as Figure 1(a) on the 768^2 mesh. Anyway, they all converge to steady state.

Figure 2 shows comparison of the temperature distributions along the front symmetry axis for $M = 3.55$ case as computed with different schemes. As the analytical solution is not available, we use the result computed by NND-LF scheme on the 1024^2 mesh as the 'exact' reference solution. One can see that the positions of the shock and deflagration fronts are different for different schemes. The shock and deflagration fronts of NND-LF, MUSCL-Roe, and TVD schemes are in turn close to the reference solution. The shocks of WENO-LF and WENO-Roe schemes are in better agreement with the reference solution, but the deflagrations by them are worse than the other three schemes.

Table I. Two typical inflow conditions in Lehr's benchmark experiments.

M	$U\ (m/s)$	a (m/s)	$D_{CJ}\ (m/s)$	T (K)	p (mmHg)	Gas mixture
3.55	1892	533	2550	293	186	H_2/O_2
6.46	2605	403	2055	293	320	H_2/air

DOI: 10.1002/fld

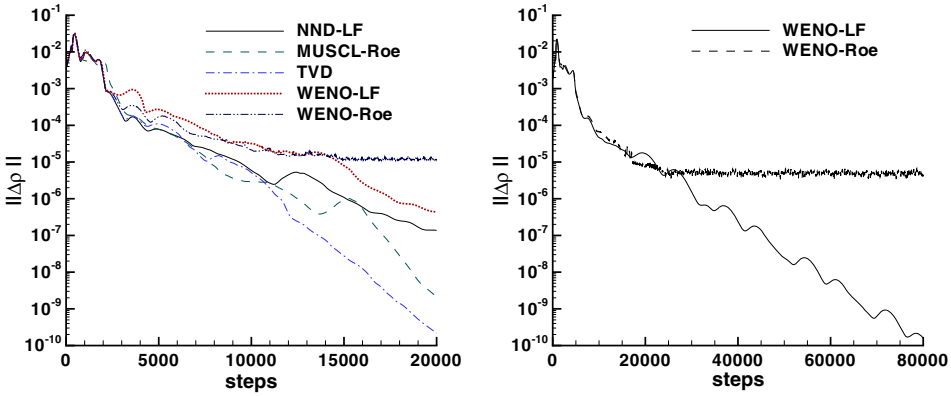

(a) 256^2 mesh (b) 512^2 mesh

Figure 1. Convergence histories of various schemes for $M = 3.55$ flow past the spherical projectile on two different meshes, CFL = 1.

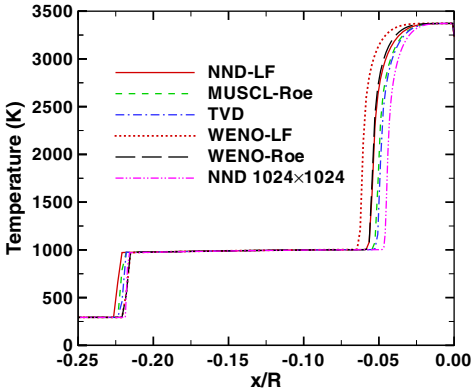

Figure 2. Axial distribution of temperature for $M = 3.55$ case on the 256^2 mesh.

This deterioration of accuracy in the combustion front is also visible in density contours shown in Figure 3. Figure 3(a–c) shows that the combustion front is normal to the symmetric axis, but Figure 3(d and e) shows that it is slightly oblique to the symmetric axis, whereas the enlarged Figure 3(f) shows that it is more abnormal for WENO-Roe with H-type fix (37). The obliqueness is a reminder of the carbuncle-like abnormality on the combustion front. WENO schemes have less dissipation than the other schemes so that they are more severely plagued by the carbuncle-like abnormality. Furthermore, certain degree of numerical oscillations occurs after the shock in the WENO results, which may further amplify combustion instability, resulting in convergence difficulty in the following $M = 6.46$ case.

Figure 4(a) shows the convergence histories for $M = 6.46$ case on the coarse 256^2 mesh. The entropy fix (37) is applied to NND-LF, MUSCL, and TVD, whereas the entropy fix (38) with $\epsilon_0 = 1$ is applied to both WENO schemes. One can observe that NND-LF, MUSCL, and TVD schemes can converge to steady states, but both WENO schemes can only drop two to three orders of magnitude even with this larger entropy correction. Their residuals always oscillate around 10^{-3} on further finer meshes and do not converge at all. However, Figure 4(b) shows that WENO schemes can converge well on the 768^2 mesh for the nonreactive case. Figure 4(c) shows that NND-LF, MUSCL, and TVD schemes can converge for the reactive case on the 512^2 mesh. On the 768^2 mesh as shown in Figure 4(d), even the most robust NND-LF scheme cannot converge irrespective of viscous, inviscid, or smaller Courant, Friedrichs and Lewy (CFL) number options.

Figure 5 shows the comparison of density contours for $M = 6.46$ case on 256^2 and 512^2 meshes. One can see that the shock and combustion locations at the outlet plane for NND-LF, MUSCL, TVD,

DOI: 10.1002/fld

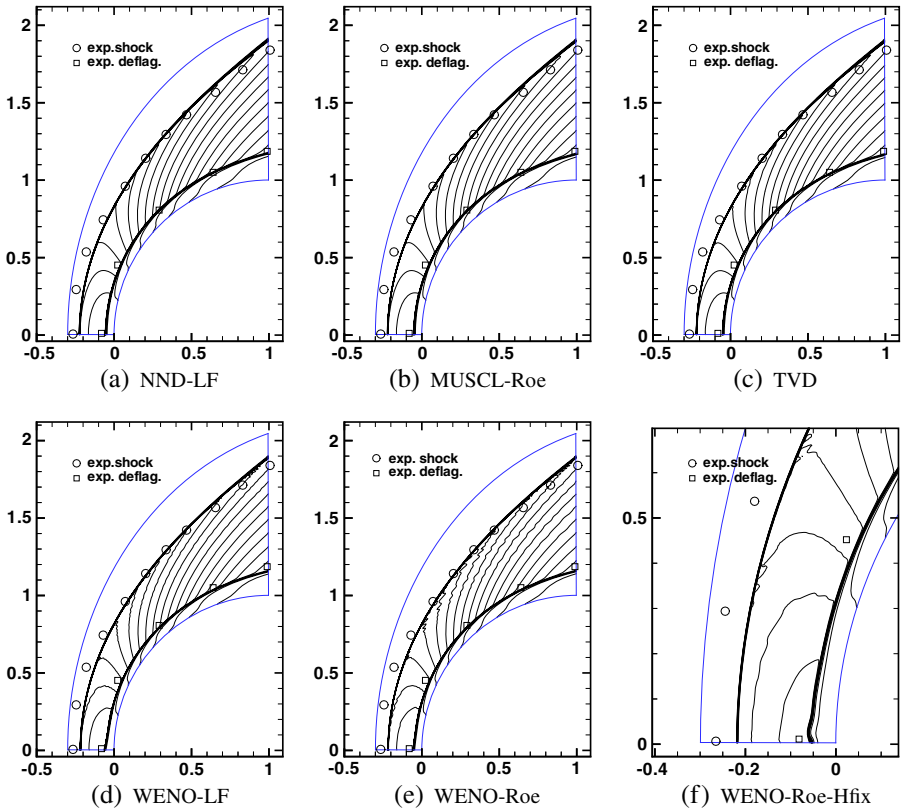

Figure 3. Density contours for $M = 3.55$ case on 256^2 mesh. Symbols are experimental [4].

WENO-LF, and WENO-Roe are in turn closer to the experimental symbols, which is in accordance with our expectation. WENO schemes have better resolution than the former three schemes on 256^2 meshes even though they have used larger entropy correction. The density contours on 512^2 meshes as computed by NND-LF, MUSCL-Roe, and TVD are much improved over those on 256^2 meshes, and differences between them are indiscernible. We show only MUSCL-Roe results in Figure 5(f).

The $M = 6.46$ case with detonation waves shows that all the five schemes do not converge on 768^2 meshes. The following case of the supersonic ram accelerator will also show that convergence difficulty occurs above 512^2 meshes.

4.2. Internal flow past a ram accelerator

The configuration of the ram accelerator [6] is composed of a tube and a projectile with diameters of 3.0 and 1.95 cm, respectively. The length of the projectile is 15 cm, and its half cone angle is 14°. The gas mixture is composed of $2H_2 + O_2 + 3.76N_2$. The boundary conditions of the inlet are the free-stream conditions: $M = 6.7$, $p_\infty = 1$ atm, $T_\infty = 300$ K. The nonslip, zero normal pressure gradient, isothermal, and noncatalytic boundary conditions are applied on the projectile's and tube's surfaces with $T_w = 600$ K. The tube wall moves at the speed of the free-stream velocity. The symmetric conditions are applied along the symmetry axis, and the zero-derivative extrapolation conditions are used for flow states at the outlet that is located 8 tube diameters downstream of the projectile.

Figure 6 shows the comparison of convergence history on different meshes. It is seen that NND-LF, MUSCL, and TVD schemes employing the H-type correction can converge on 256^2 and 384^2 meshes. However, WENO-LF and WENO-Roe schemes must employ larger entropy correction to ensure convergence on 256^2 meshes. The residual of WENO-Roe blows up on 384^2 meshes, and all the schemes are either oscillatory or diverge on 512^2 meshes. This numerical divergence may be

DOI: 10.1002/fld

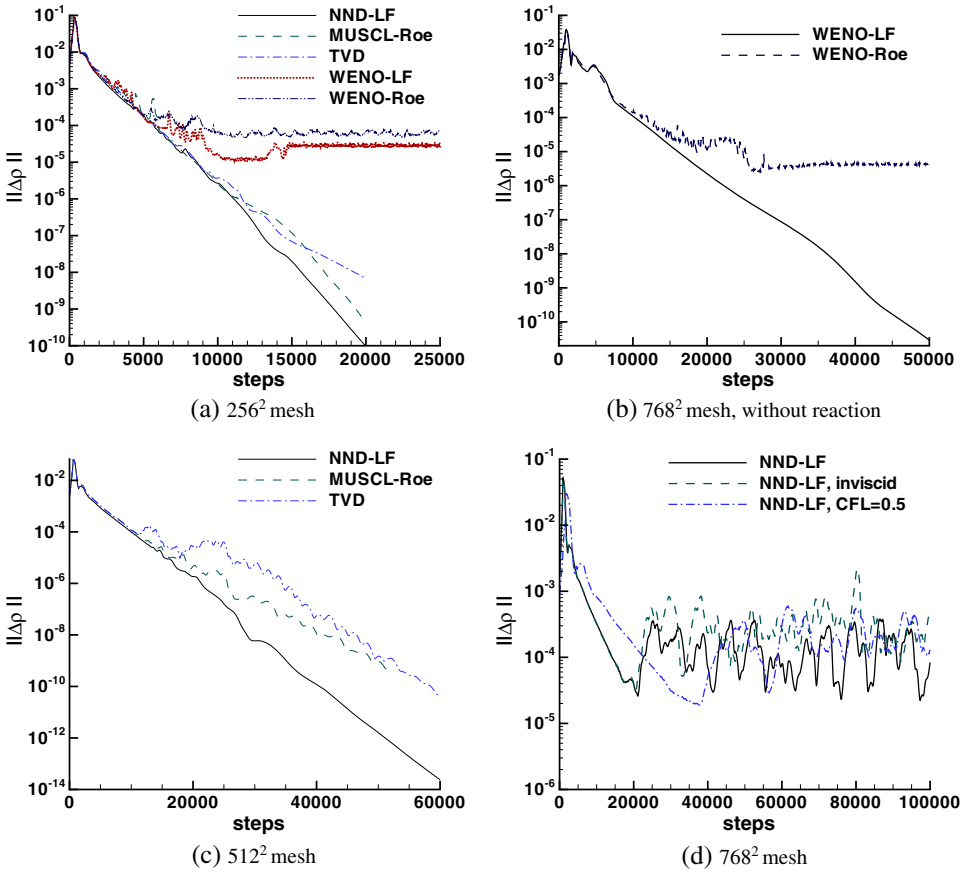

(a) 256^2 mesh (b) 768^2 mesh, without reaction

(c) 512^2 mesh (d) 768^2 mesh

Figure 4. Convergence histories on different mesh sizes for $M = 6.46$ case, CFL $= 1$.

related to a physical phenomenon called 'unstart' for supersonic ram accelerator flow, in which a detonation wave is formed in front of the projectile and the projectile is retarded instead of thrusted. When the detonation moves upstream of the inlet boundary, computation always overflows because of inappropriate boundary conditions applied.

Figure 7 shows the comparison of pressure contours between various schemes on three mesh sizes. The converged results on 256^2 and 384^2 meshes for NND-LF, MUSCL-Roe, and TVD schemes are close to one another, which illustrate that there is a detonation wave at the start of the throat, whereas the converged WENO results on 256^2 meshes and the unconverged MUSCL-Roe results on 512^2 meshes all show a detonation wave at further upstream position. The convergence on coarse to medium meshes but nonconvergence on finer meshes reflects that there are special difficulties in calculating some steady-state shock-induced combustion problems.

4.3. Discussions

Failure to converge to steady states on fine meshes is not scarce in flow simulation, but it needs attention. There are two categories of mechanisms for this, one is physical, another is numerical. The benchmark problem of $M = 3$ supersonic flow past a forward step in a channel that belongs to the first category, where transitions from steady state to unsteadiness can be triggered by instability of the contact discontinuity. This results in failure to converge for a steady solver, as finer and finer vortices occur on gradually refined meshes in previous simulation [44]. But present $M = 6.46$ case seems to be of the second category, as experimental picture [4] shows that there is no observable unsteadiness for the shock and the combustion fronts, whereas our unconverged density contours have false unsteady patterns (not shown in this paper). We are not sure whether $M = 6.7$ case is

DOI: 10.1002/fld

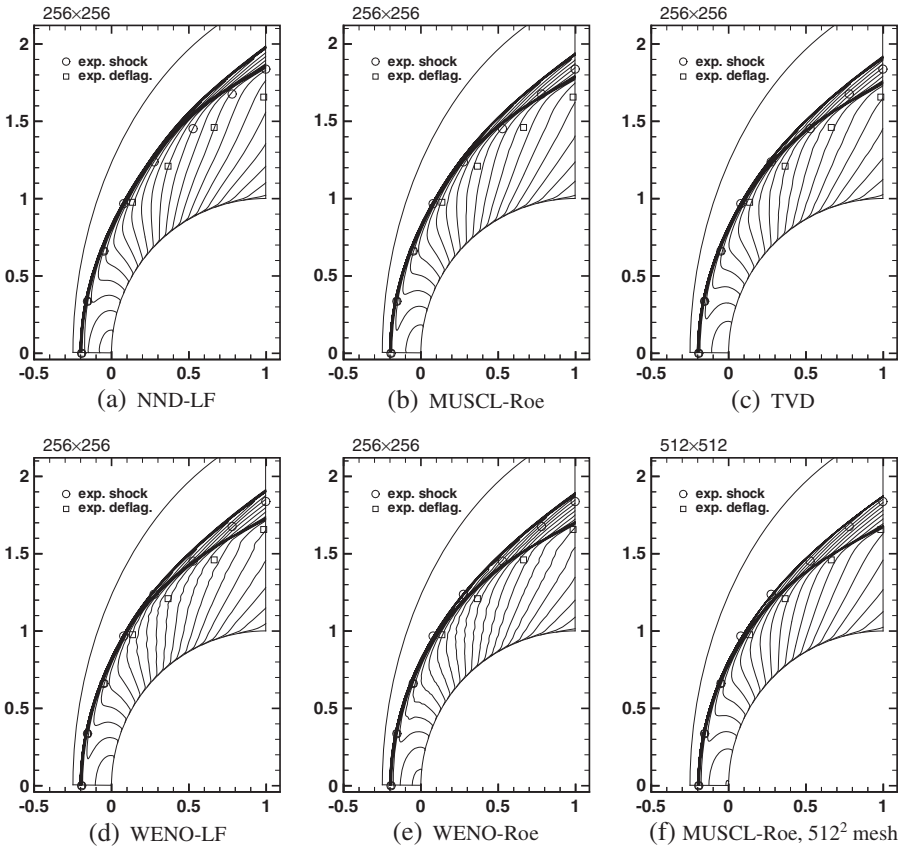

Figure 5. Density contours for $M = 6.46$ flow past a hemisphere on 256^2 and 512^2 meshes. Symbols are experimental [4].

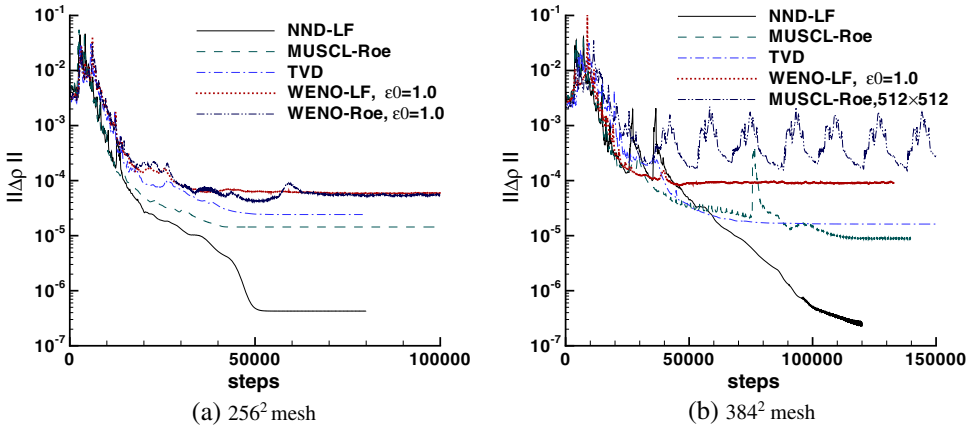

Figure 6. Convergence histories on different meshes for $M = 6.7$ ram accelerator flow. CFL numbers vary from 0.2 to 0.5 for different schemes.

steady or not. The two cases were thought to be steady-state flows based on coarse to medium mesh simulation in quite a few papers [6, 7, 9].

We have conducted both viscous and inviscid simulations and used different CFL numbers as demonstrated in Figure 4(d), but results on the 768^2 fine mesh are still not converged. It is noted that we also used Jachiomowski's reaction mechanism, yet the residuals did not converge just on a finer mesh like 1024^2. This means that the bad convergence on fine meshes may come from the

DOI: 10.1002/fld

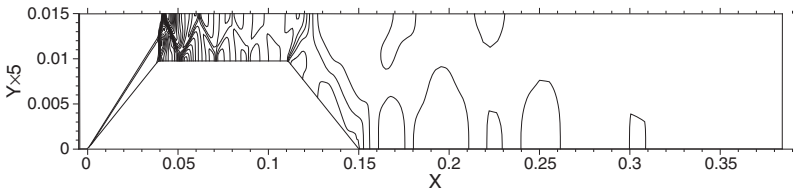

(a) NND-LF, 256^2 mesh

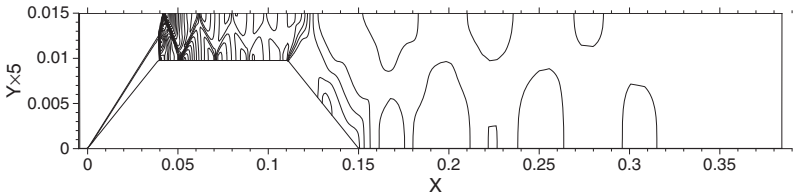

(b) MUSCL-Roe, 256^2 mesh

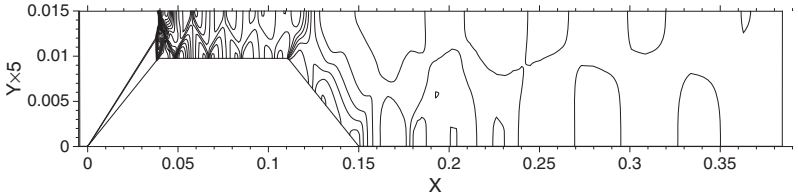

(c) TVD, 256^2 mesh

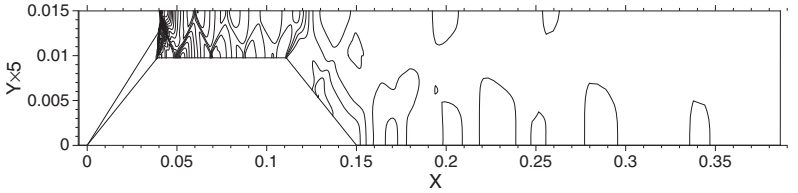

(d) MUSCL-Roe, 384^2 mesh

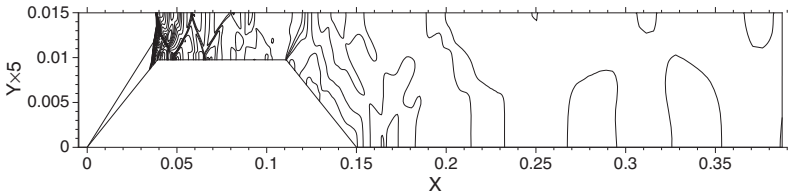

(e) MUSCL-Roe, 512^2 mesh, unconverged

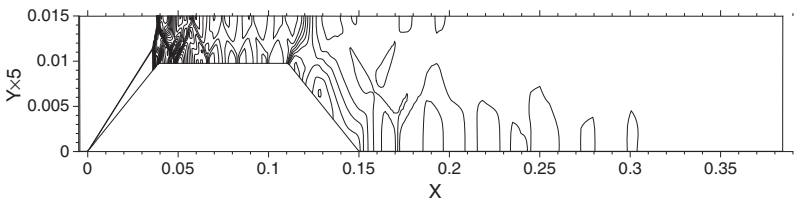

(f) WENO-LF, 256^2 mesh

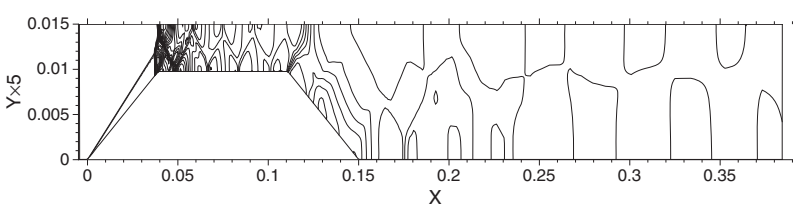

(g) WENO-Roe, 256^2 mesh

Figure 7. Pressure contours for $M = 6.7$ flow in a ram accelerator.

DOI: 10.1002/fld

poor numerical treatment of the stiff nonlinear chemical source terms, particularly the coupling of shock and deflagration as in $M = 6.46$ and 6.7 cases. However, we have not tested other numerical remedies like a robust preconditioned solver that is capable of overcoming matrix stiffness rather than the LU–SGS scheme and a new scheme that can reflect the mechanism of the hydrodynamic–chemical interactions correctly. Finally, if these optional remedies do not work for $M = 6.46$ and 6.7 reactive cases, then one must use a DNS solver with very dense meshes to resolve detonation, shock, combustion, and diffusion zones to obtain statistically converged results.

5. CONCLUSIONS

We have compared numerical performance of five high-resolution schemes for computing presumedly steady-state shock-induced combustion problems using gradually refined meshes. It is concluded that all these schemes can converge to steady-state solutions for nonreacting flows and simple reacting flows without shock–deflagration interactions using as fine as 768^2 meshes. The robustness of convergence in descending order are NND-LF, MUSCL-Roe, Harten–Yee TVD, WENO-LF, and WENO-Roe. For cases where shock and deflagration fronts have coupling and separation, even if the robust NND, MUSCL, and TVD schemes can obtain steady-state solutions on coarse to medium meshes, they cannot converge to steady states on even finer meshes. Obtaining grid-independent steady solutions for such cases is very difficult if not impossible. Before more sophisticate DNS approach is invoked to obtain statistically converged results, we wish to use a more robust preconditioned solver than the LU–SGS scheme, which may overcome matrix stiffness on fine meshes, and develop new scheme that can model the intricate mechanism of hydrodynamic–chemical interactions correctly. These will be for future work.

ACKNOWLEDGEMENTS

The authors thank Drs Wei Liu and Lei Zhang for useful discussions and valuable comments from referees on entropy fix. This work was supported by the Natural Science Foundation of China (10972230, 11021101) and state key program for developing basic sciences (2010CB731505).

REFERENCES

1. Shepherd JE. Detonation waves and propulsion. In *Combustion in High Speed Flows*. Kluwer Academic Publishers: Dordrecht, 1994; 373–420.
2. Bdzil JB, Stewart DS. The dynamics of detonation in explosive systems. *Annual Review of Fluid Mechanics* 2007; **39**:263–292.
3. Oran ES, Boris JP. *Numerical Simulation of Reactive Flow*. Elsevier: New York, 1987. Chap.13.
4. Lehr HF. Experiments on shock-induced combustion. *Astronautica Acta* 1972; **17**:589–597.
5. McVey JB, Toong TY. Mechanism of instabilities of exothermic hypersonic blunt-body flows. *Combustion Science and Technology* 1971; **3**(2):63–79.
6. Yungster S, Eberhardt S, Bruckner A. Numerical simulation of hypervelocity projectiles in detonable gases. *AIAA Journal* 1991; **29**(2):187–199.
7. Matsuo A, Fujii K. Flow features of shock-induced combustion around projectile travelling at hypervelocities. *AIAA Journal* 1995; **33**(6):1056–1063.
8. Clutter K, Krishnamurty V, Shyy W. Combustion and turbulent effects in hypersonic projectile flows. *AIAA Paper 97–0897*, 1997.
9. Yuan L, Tang T. Resolving the shock-induced combustion by an adaptive mesh redistribution method. *Journal of Computational Physics* 2007; **224**(2):587–600.
10. Harten A. High resolution schemes for hypersonic conservation laws. *Journal of Computational Physics* 1983; **49**(3):357–393.
11. Greene FA, Gupta RU. Viscous equilibrium computations using LAURA. *Journal of Spacecraft and Rockets* 1992; **29**(5):627–632.
12. Van Leer B. Towards the ultimate conservation difference scheme V: a second-order sequel to Godunov method. *Journal of Computational Physics* 1979; **32**(1):101–136.
13. Lapps T, Leonard A, Dimotakis PE. Adaptive Lagrangian method for computing 1D reacting and non-reacting flows. *Journal of Computational Physics* 1993; **104**(2):361–376.
14. Zhang HX, Zhuang FG. NND schemes and their application to numerical simulation of two-dimensional and three-dimensional flows. *Advances in Applied Mechanics* 1992; **29**:193–256.

DOI: 10.1002/fld

15. Ouyang SW, Xie ZQ. Numerical solution of the Navier–Stokes equations for three-dimensional hypersonic chemically nonequilibrium flows. *Acta Mechanica Sinica* 1996; **28**(1):90–98. (In Chinese).
16. Harten A, Engquist B, Osher S. Unifomrly high-order accurate essentially non-oscillatory schemes III. *Journal of Computational Physics* 1987; **71**(2):231–303.
17. Liu XD, Osher S, Chan T. Weighted essentially non-oscillatory schemes. *Journal of Computational Physics* 1994; **115**(1):200–212.
18. Xu SJ, Aslam T, Stewart DS. High resolution numerical simulation of ideal and non-ideal compressible reacting flows with embedded internal boundaries. *Combustion Theory Modelling* 1997; **1**:113–142.
19. Hu XY, Khoo BC, Zhang DL, Jiang ZL. The cellular structure of a two dimensional H2/O2/Ar detonation wave. *Combustion Theory and Modelling* 2004; **8**(2):339–359.
20. Wei W, Chi-Wang S, Yee HC, Sjögreen B. High order finite difference methods with subcell resolution for advection equations with stiff source terms. *Journal of Computational Physics* 2012; **231**(1):190–214.
21. Liou MS. Ten years in the making-AUSM family. *AIAA Paper 2001–2521*, 2001.
22. Gao TS, Lee CH, Dong WZ, Zhang QY. Numerical simulation of hypersonic ionized airflow. *Acta Aerodynamica Sinica* 2002; **20**(2):185–191. (In Chinese).
23. Chang SC, Wang XY, Chow CY. The space-time conservation element and solution element method: a new high–resolution and genuinely multidimensional paradigm for solving conservation laws. *Journal of Computational Physics* 1999; **156**(1):89–136.
24. Wang G, Zhang DL, Liu KX, Wang JT. An improved CE/SE scheme for numerical simulation of gaseous and two-phase detonations. *Computers & Fluids* 2010; **39**(1):168–177.
25. Cockburn B, Shu CW. Runge–Kutta discontinuous Galerkin methods for convection-dominate problems. *Journal of Scientific Computing* 2001; **16**(3):173–261.
26. Billet G, Ryan J. A Runge–Kutta discontinuous Galerkin approach to solve reactive flows: the hyperbolic operator. *Journal of Computational Physics* 2011; **230**(4):1064–1083.
27. Zhang L, Yuan L. Runge–Kutta discontinuous Galerkin method for detonation waves. *Chinese Journal of Computational Physics* 2009; **27**(4):509–517. (In Chinese).
28. Pirozzoli S. Numerical methods for high-speed flows. *Annual Review of Fluid Mechanics* 2011; **43**(2):163–194.
29. Ziegler JL, Deiterding R, Shepherd JE, Pullin DI. An adaptive high-order hybrid scheme for compressive, viscous flows with detailed chemistry. *Journal of Computational Physics* 2011; **230**:7598–7630.
30. Roe PL. Approximate Riemann solvers, parameter vectors, and difference schemes. *Journal of Computational Physics* 1981; **43**(2):357–372.
31. Shu CW. Essentially non-oscillatory and weighted essentially non-oscillatory schemes for hyperbolic conservation laws. *ICASE Report No. 97–65*, 1997.
32. Jiang GS, Wu CC. A high-order WENO finite difference scheme for the equations of ideal magnetohydrodynamics. *Journal of Computational Physics* 1999; **150**(2):561–594.
33. Yee HC. A class of high-resolution explicit and implicit shock-capturing methods. *NASA TM 101088*, 1989.
34. Yoon S, Jameson A. Lower–upper symmetric Gauss–Seidel method for the Euler and Navier–Stokes equations. *AIAA Journal* 1988; **26**(19):1025–1026.
35. Shuen J, Yoon S. Numerical study of chemically reacting flows using a lower–upper symmetric successive overrelaxation scheme. *AIAA Journal* 1989; **27**(12):1752–1760.
36. Kee RJ, Rupley FM, Meeks E, Miller JA. Chemkin-III: a Fortran chemical kinetics package for the analysis of gas-phase chemical and plasma kinetics. *UC405, SAND 96–8216*, 1996.
37. Gupta RN, Yos JM, Thompson RA. A review of reaction rates and thermodynamic and transport properties for the 11-species air model for chemical and thermal nonequilibrium calculations to 30000K. *NASA TM 101528*, 1989.
38. Bhutta BA, Lewis CH. A new technique for low-to-high altitude predictions of ablative hypersonic flowfields. *AIAA-91-1392*, 1991.
39. Sanders R, Morano E, Druguett MC. Multidimensional dissipation for upwind schemes: stability and applications to gas dynamics. *Journal of Computational Physics* 1998; **145**(2):511–537.
40. Cheatwood FM, Gnoffo PA. User's manual for the Langley aerothermodynamic upwind relaxation algorithm (LAURA). *NASA TM 4674*, 1996.
41. Gross A, Fasel HF. High-order-accurate numerical method for complex flows. *AIAA Journal* 2008; **46**(1):204–214.
42. Henrick AK, Aslam TD, Powers JM. Mapped weighted essentially non-oscillatory schemes: achieving optimal order near critical points. *Journal of Computational Physics* 2005; **207**:542–567.
43. Evans JS, Schexnayder CJ. Influence of chemical kinetics and unmixedness on burning in supersonic hydrogen flames. *AIAA Journal* 1980; **18**(2):188–193.
44. Zhu J, Qiu JX. Trigonometric WENO schemes for hyperbolic conservation laws and highly oscillatory problems. *Communications in Computational Physics* 2010; **8**(5):1242–1263.

DOI: 10.1002/fld